Supporting Information for

Correlated terahertz phonon-ion interactions control ion conduction in a solid electrolyte

Kim H. Pham[1†], Kiarash Gordiz[2†], Natan A. Spear[3†], Amy K. Lin[1], Jonathan M. Michelsen[1], Hanzhe Liu[1], Daniele Vivona[2], Geoffrey A. Blake[4], Yang Shao-Horn[2,5], Asegun Henry[2], Kimberly A. See[1], Scott K. Cushing[1*]

[†]These authors contributed equally to this work, ¶Corresponding author

[1]Division of Chemistry and Chemical Engineering, California Institute of Technology, Pasadena, California 91125, United States [2]Department of Mechanical Engineering, Massachusetts Institute of Technology, Cambridge, Massachusetts 02139, United States [3]Department of Applied Physics and Materials Science, California Institute of Technology, Pasadena, California 91125, United States [4]Division of Geological and Planetary Sciences, California Institute of Technology, Pasadena, California 91125, United States [5]Research Laboratory of Electronics, Massachusetts Institute of Technology, Cambridge, Massachusetts 02139, United States *Correspondence to: scushing@caltech.edu

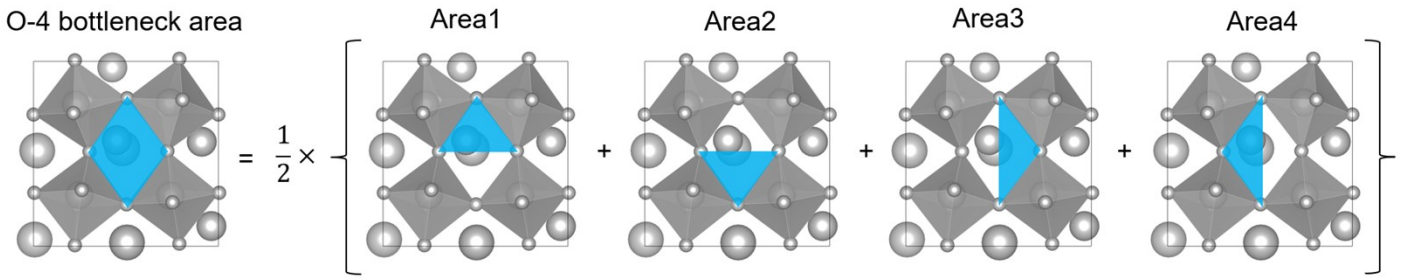

Figure S1. The O-4 bottleneck area in space is approximated by averaging over four smaller triangular areas (shown by blue).

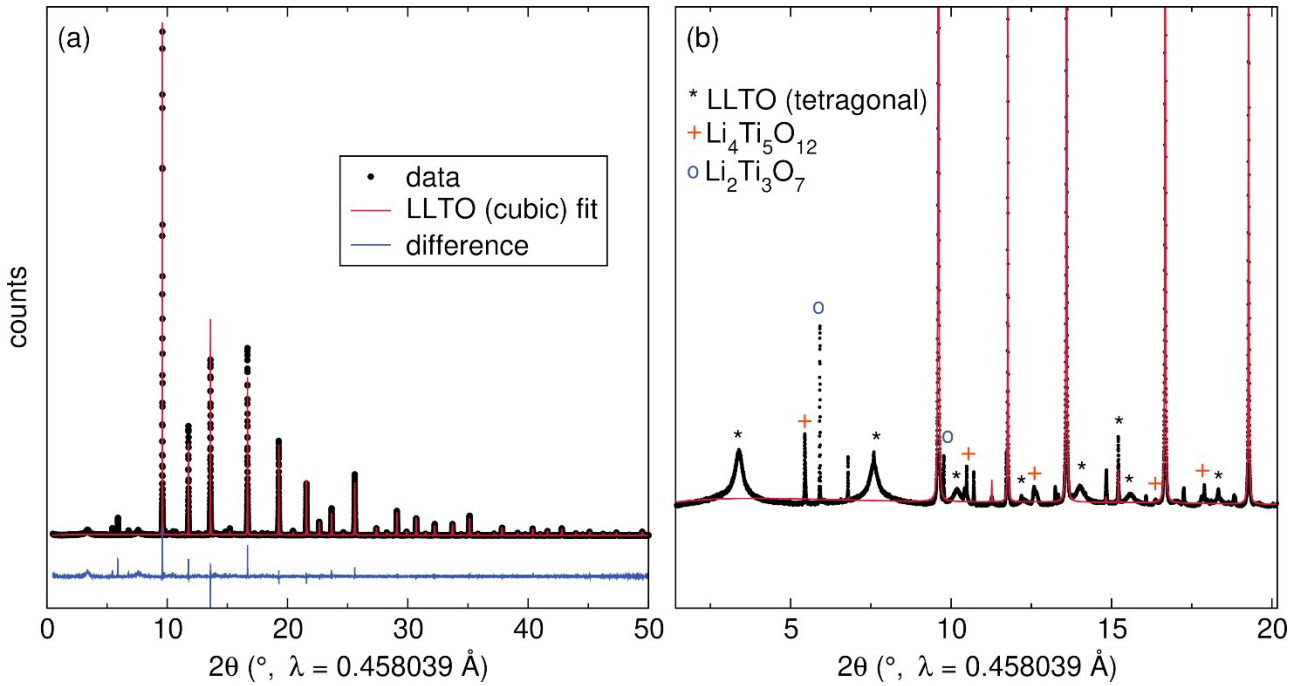

Figure S2. Synchrotron X-ray diffraction of LLTO. (a) Quantitative Rietveld refinement to the cubic phase of LLTO describes the data well. (b) The small peaks at low angle are associated with both the tetragonal phase of LLTO, which includes ordered La – a common phenomenon[1] – and some Li-Ti-O impurity phases. A four-phase fit to the data (not shown) suggests the impurity phases are much less than 8 wt% of the material. Additionally, no impurity phases are visible in the Raman spectrum (**Fig. 5**).

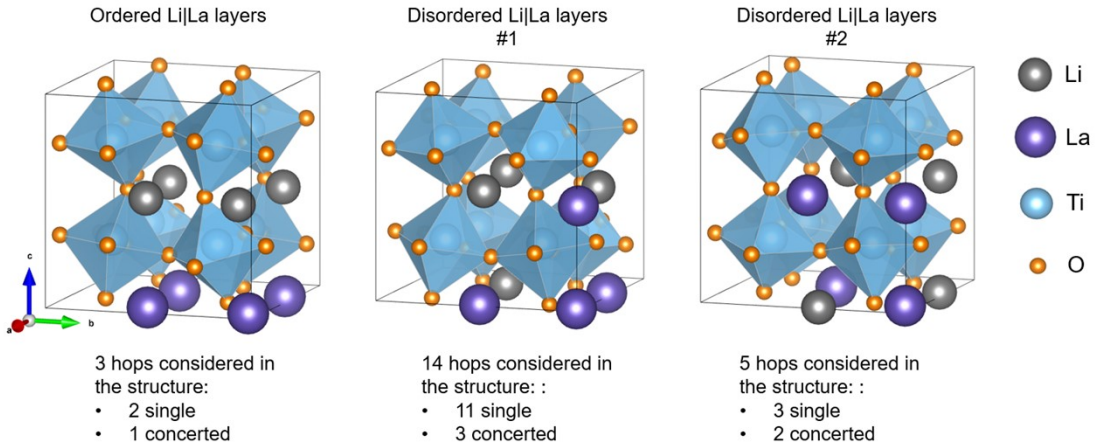

Figure S3. Schematics of three different Li|La orderings with respect to the c-axis in the $Li_{0.5}La_{0.5}TiO_3$ lattice included in our calculations. The chosen number of Li^+ ion hops with different hopping mechanisms are also included in the bottom of the schematics.

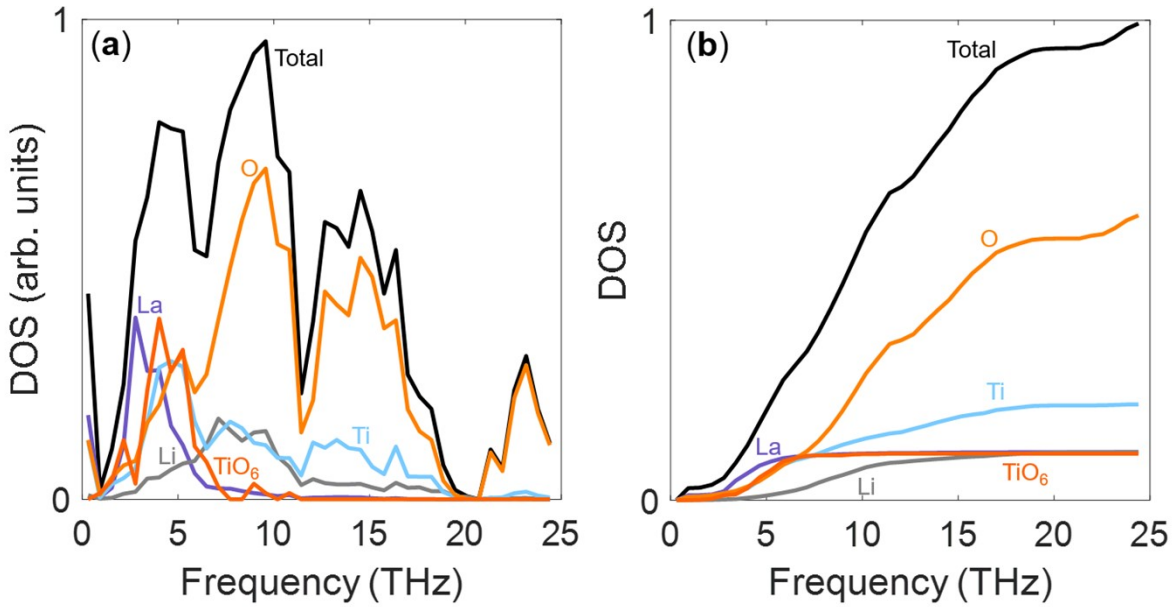

Figure S4. Total and partial phonon density of states in (a) non-accumulation and (b) accumulation format for different atomic species and rocking modes (TiO_6 units), showing that that 10 % of the total modes are of TiO_6 rocking nature, and in the <6THz region, 36% of the modes are of TiO_6 rocking nature.

Table S1. Enhancement in the ion hopping rate by targeted excitation of the highest contributing non-rocking mode, highest contributing rocking mode, and one random mode, that have frequencies in the experimentally accessible frequency range, during MD simulations. The targeted excitation of phonons during MD simulation is explained in the **Methods** and the method is applied to three hops among the hops investigated in this study. The visualization of these hops is provided in **Fig. S5**. The numbers included in the table are ion hopping rates (#jumps/ps). Following the sorted phonon contributions shown in **Fig. S7**, almost 50% of the existing phonons in the structure do not have any noticeable contribution to the Li^+ ion hop in the lattice, based on which, they can be categorized/labeled as "random" as opposed to their "highly contributing" counterparts.

			400 K (natural MD simulation)	700 K (natural MD simulation)	400 K (with mode excited to 700 K)
Hop #1	Jump rate (#jumps/ps)	Highest non-rocking-mode contributing mode (4.29 THz)	0.0011	1.45	1.27
		Highest rocking-mode contributing mode (3.46 THz)			1.39
		Random mode (2.66 THz)			0.0027
Hop #2	Jump rate (#jumps/ps)	Highest non-rocking-mode contributing mode (4.50 THz)	0.0024	2.07	3.61
		Highest rocking-mode contributing mode (1.84 THz)			3.23
		Random mode (3.47 THz)			0.0004
Hop #3	Jump rate (#jumps/ps)	Highest non-rocking-mode contributing mode (5.10 THz)	0.0017	1.44	2.09

		Highest rocking-mode contributing mode (1.94 THz)			1.94
		Random mode (4.43 THz)			0.0011

Figure S5. The schematic of the three hops discussed in **Table S1**, with structures at the beginning, during, and end of the hop displayed in both standard view (upper panel) and top view (bottom panel). The "during the hop" representation depicts the hopping atom's different positions during the hop. The bottleneck of the hop is formed by four O atoms (O-4), indicated by black lines in the "during the hop" representation, and an assisted view is provided for better visualization of the bottleneck area. The relative energies corresponding to the minimum energy pathway are displayed in the bottom-right panel.

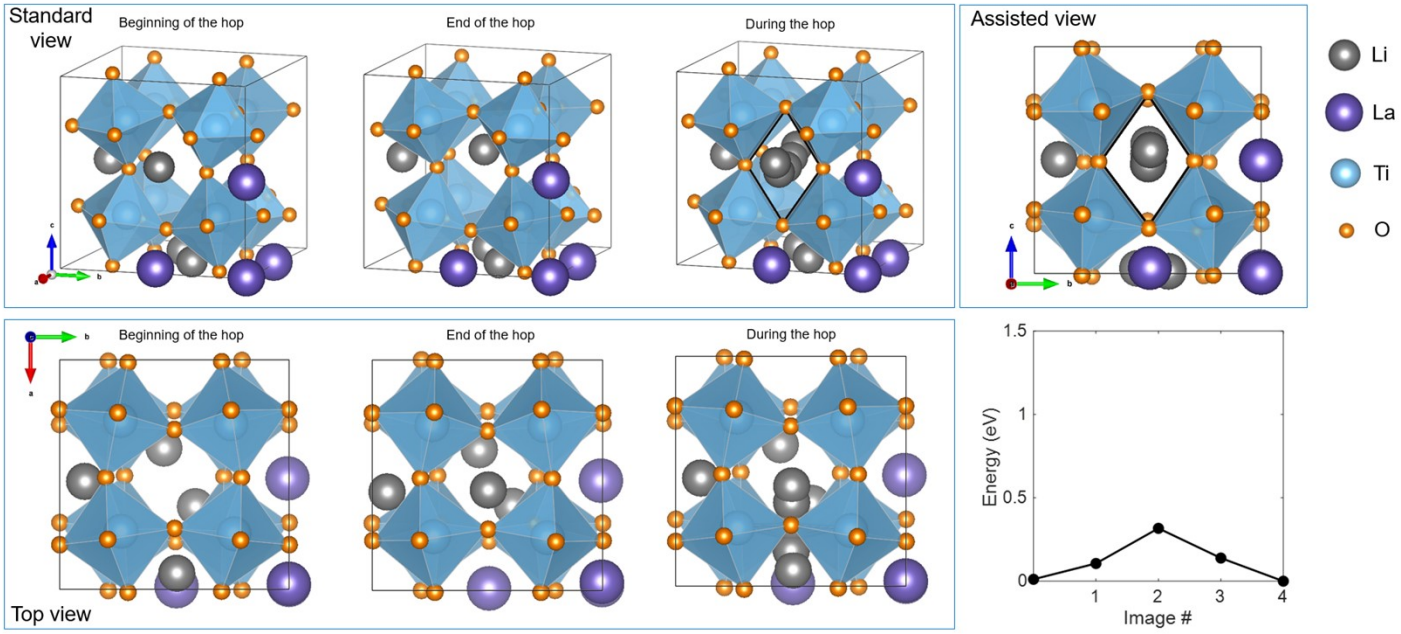

Figure S5.1. Representation of Hop #1. The shown hop is a single ion hop, and the structure is derived by repositioning of the Li atoms in the parent disordered structure #1 shown in **Fig. S3**. This hop is also described in **Fig. 2** and **Table 1** in the main manuscript.

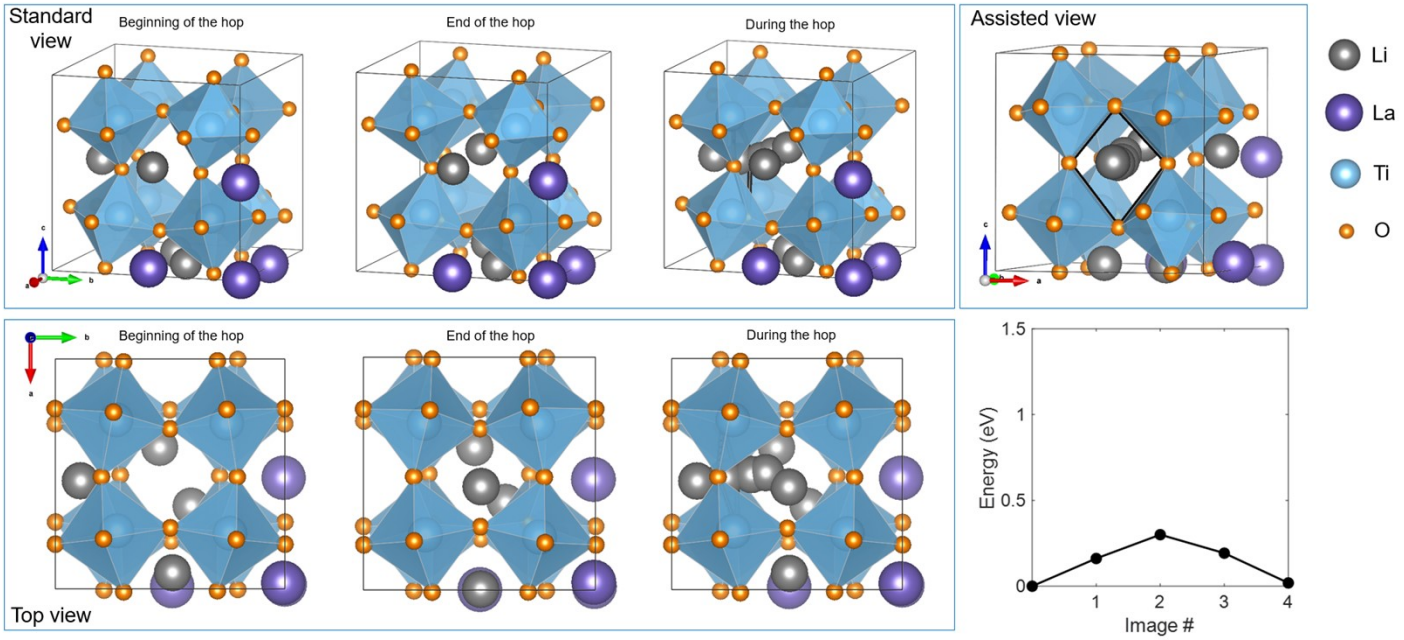

Figure S5.2. Representation of Hop #2. The shown hop is a single ion hop, and the structure is derived by repositioning of the Li atoms in the parent disordered structure #1 shown in **Fig. S3**.

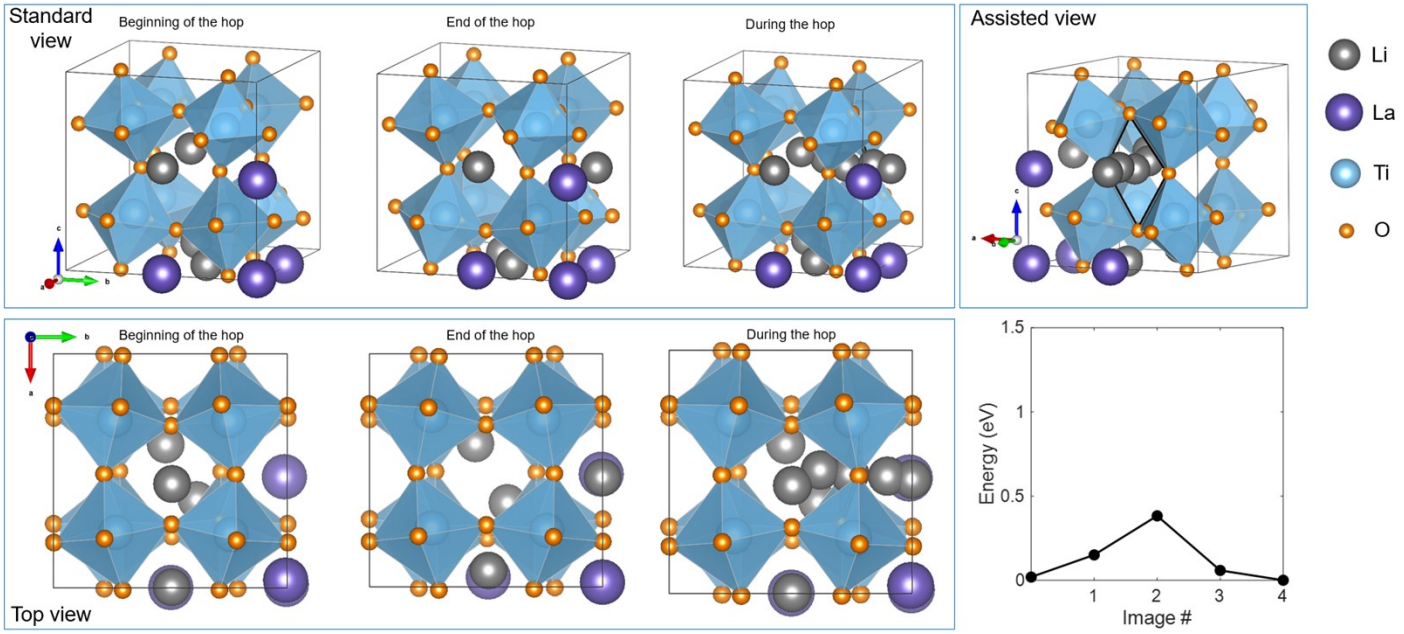

Figure S5.3. Representation of Hop #3. The shown hop is a single ion hop, and the structure is derived by repositioning of the Li atoms in the parent disordered structure #1 shown in **Fig. S3**.

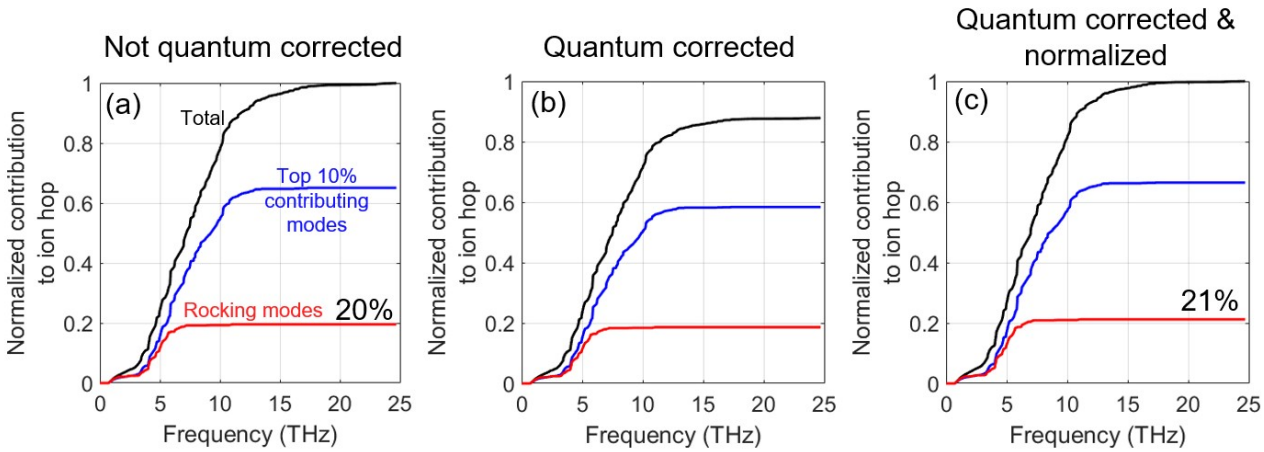

Figure S6. Effect of quantum correction on the calculated modal contributions to Li^+ hop in the LLTO lattice. The accumulative modal contributions (a) before, and (b) after quantum correction. (c) Shows the accumulative modal contributions after quantum correction, when the calculated modal contributions are normalized. It can be seen that, since most of the TiO_6 rocking modes have low frequencies (< 6 THz), correcting their contribution based on Bose Einstein distribution only slightly increases their overall percentage of contribution to Li^+ in the LLTO lattice (from 20% to 21%).

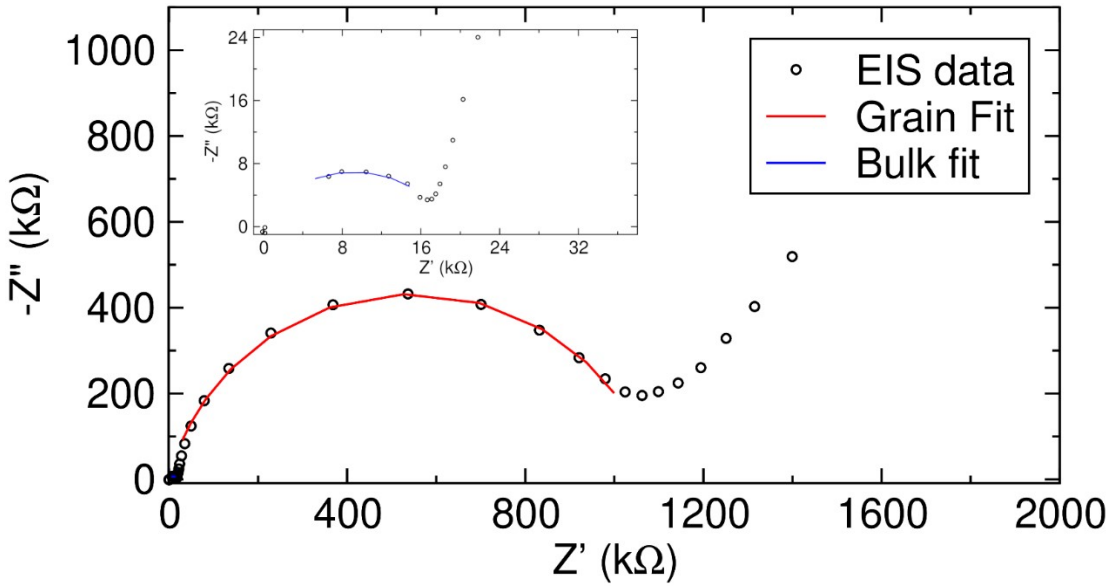

Figure S7. Full EIS spectra of LLTO with bulk and grain fits showing the bulk and grain features which are characteristic of LLTO samples, measured between 32 MHz and 1 Hz.

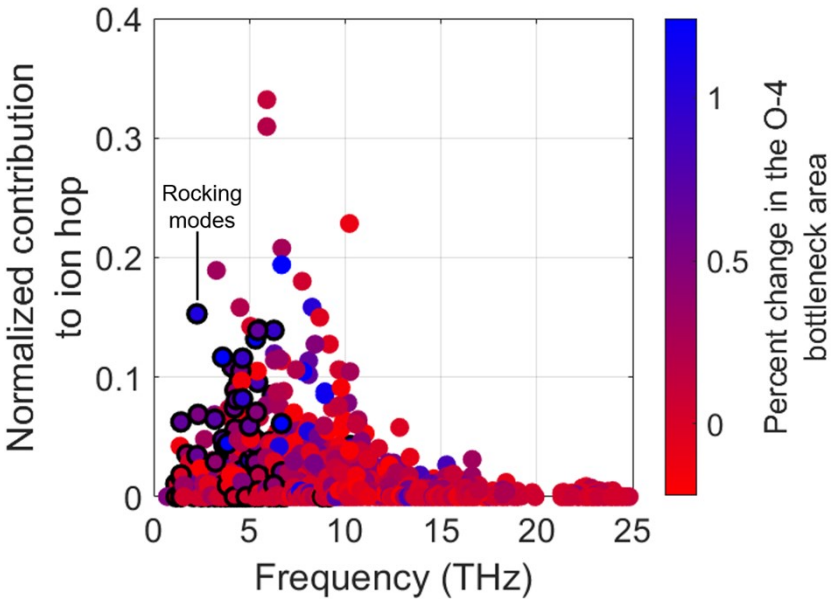

Figure S8. Scatter plot displaying the normalized individual contributions of phonons to the Li^+ ion hop in the LLTO lattice. The color of each data point represents the extent to which the corresponding phonon can modify the O-4 bottleneck area against the hopping of Li^+ ions in the lattice, with the color bar indicating the percentage of change in the bottleneck area, calculated using the methodology explained in the **Methods**. Positive percent changes refer to widening of the bottleneck while negative percent changes refer to shrinkage of the bottleneck. Rocking modes, indicated by black rings surrounding their data points, exhibit a comparatively higher ability to modify the O-4 bottleneck area in comparison to non-rocking modes.

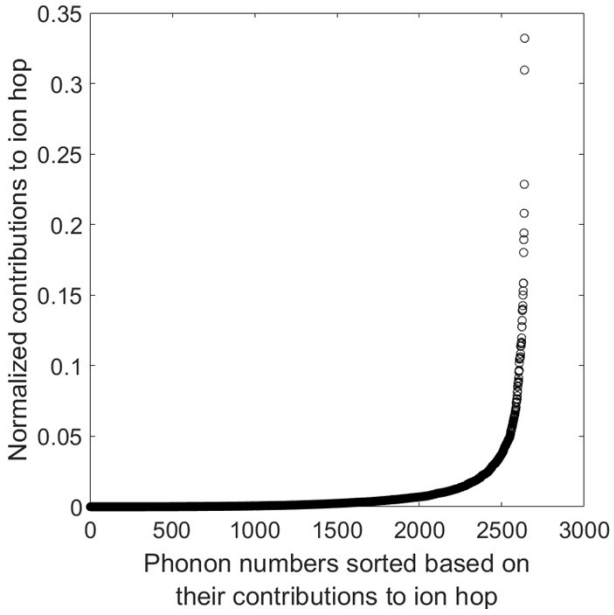

Figure S9. Sorted normalized phonon contributions to ion hop. This plot is the same as the scattered plot in **Fig. S8**, except that the phonons are sorted based on their normalized contributions to ion hop. The x-axis goes from 1 to 2640, which is the total number of vibrational modes that the contributions of which were investigated in this study: (22 hops) × (40 atoms) × (3 degrees of freedom for each atom) = 2640.

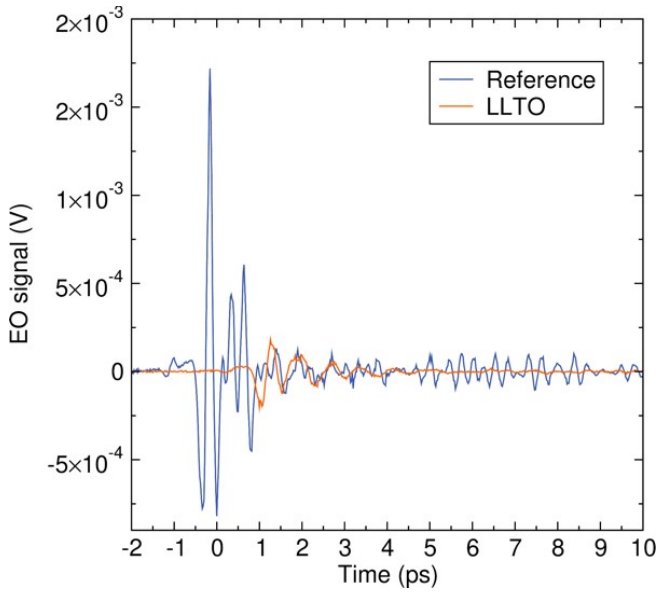

Figure S10. THz time domain trace with and without LLTO. The drop in EO signal with the LLTO sample indicates the absorption of the THz field by the sample. The generation process for this signal is described in the **Methods** section.

Table S2. The average change and standard deviations for R_{bulk} under THz illumination at each of the measured powers with three trials at each power across four samples. We note the large standard deviations, particularly at low laser power, are due to instability in the laser source coupled with variations in R_{bulk} across different samples and between trials.

Laser power (mW)	ΔR_{bulk} (Ω)	Standard deviation in ΔR_{bulk} (Ω)
0.24	24.1	46.6
0.57	72.8	55.6
0.90	114	24.7
1.3	195	54.9
1.6	258	126

Table S3. The average change and standard deviations for R_{bulk} under 800 nm laser illumination at each of the measured powers with four trials at each power across three samples. We note the large standard deviations stem from instabilities in the laser power and variations in the absolute value of in R_{bulk} across different samples and between trials.

Laser power (mW)	ΔR_{bulk} (Ω)	Standard deviation in ΔR_{bulk} (Ω)
5	144	61.7
10	335	192
15	373	197
20	582	258
25	625	306

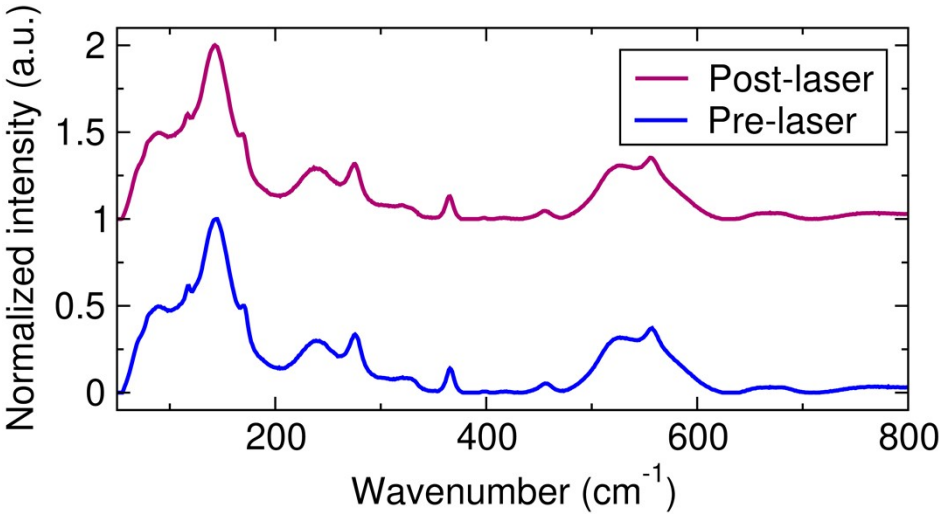

Figure S11. Raman spectra of LLTO taken before and after laser excitation on the same spot. One can see that there is no change in the Raman before and after excitation, ruling out sample damage.

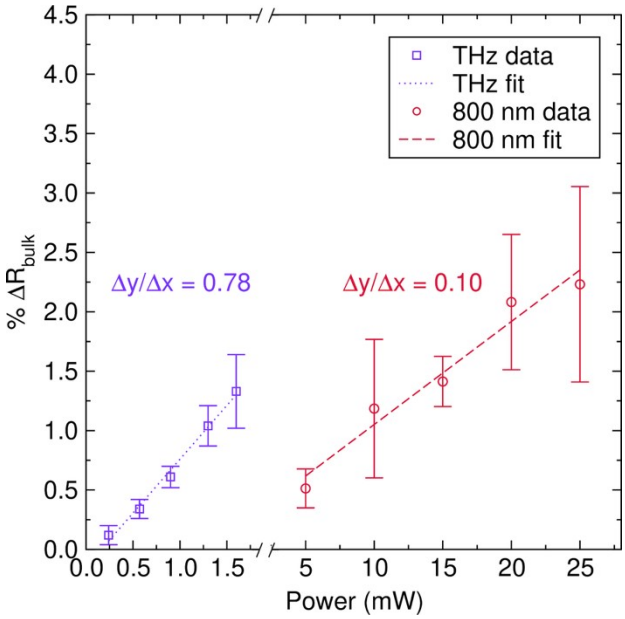

Figure S12. The shift in R_{bulk} for 800 nm and THz light excitation. The shifts in impedance from **Fig. 3** plotted against power with equal spot sizes of 250 μm, showing a 0.78% percent decrease in bulk resistance per mW of power for the THz light excitation ($R^2 = 0.9918$) and a 0.10% change in bulk resistance per mW of power for the 800 nm light excitation ($R^2 = 0.9905$).

Figure S13. The pellets used for laser-driven EIS experiments. The sputtered gold electrodes demonstrate the in-plane electrode geometry where the light excitation was focused directly between the two electrodes.

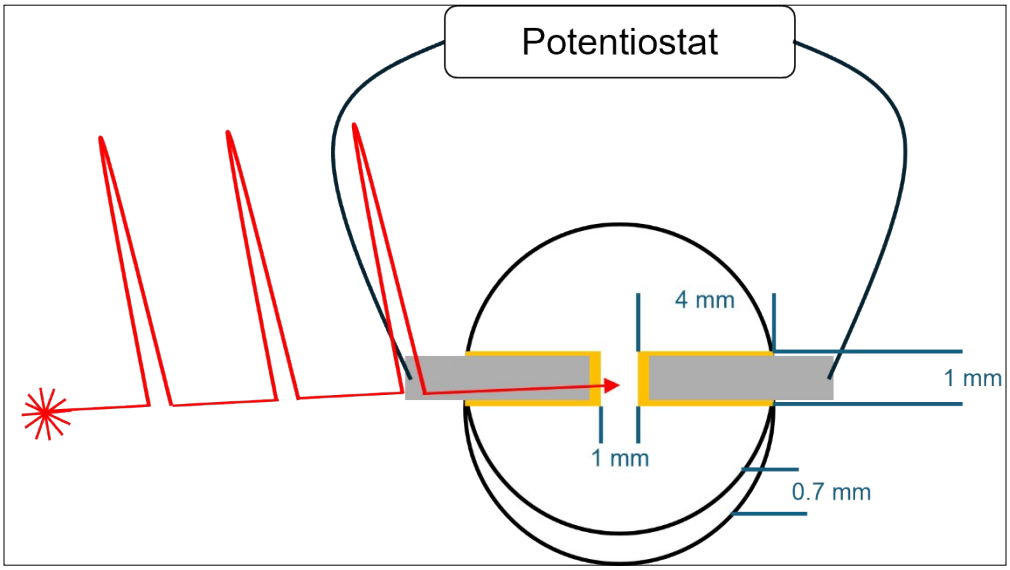

Figure S14. A graphical depiction of the laser-driven EIS experiments where the laser (in red) excites a 1 mm gap between two Au-sputtered electrodes which are 4 mm in diameter and 1 mm in width. The sample itself is 0.7 mm thick with a 9 mm radius. The Au-sputtered electrodes make electrochemical contact with stainless steel electrodes that are connected to a potentiostat which records the laser-modulated EIS signal.

Table S4. The summary of laser excitation and alternating current (AC) field parameters used for each experiment presented in this work. This incorporates differences in repetition rate and spot size for each experiment.

Experiment	**Wavelength**	**Laser fluence (mJ/cm²)**	**Average power density (mW/cm²)**	**AC Frequency (Hz)**	**AC Sinus Amplitude (mV)**
Laser-driven EIS	800 nm	10.2-50.9	$1.01*10^4$-$5.09*10^4$	$1-32*10^6$	50-100
Laser-driven EIS	0.7-4.5 THz (67-428 μm)	1.96-13.0	$488-3.26*10^3$	$1-32*10^6$	50-100
LUIS	800 nm	16.3	$8.15*10^3$	$19*10^9$	178
LUIS	0.5-5.5 THz (54.5-599 μm)	2.70	$1.25*10^3$	$19*10^9$	178

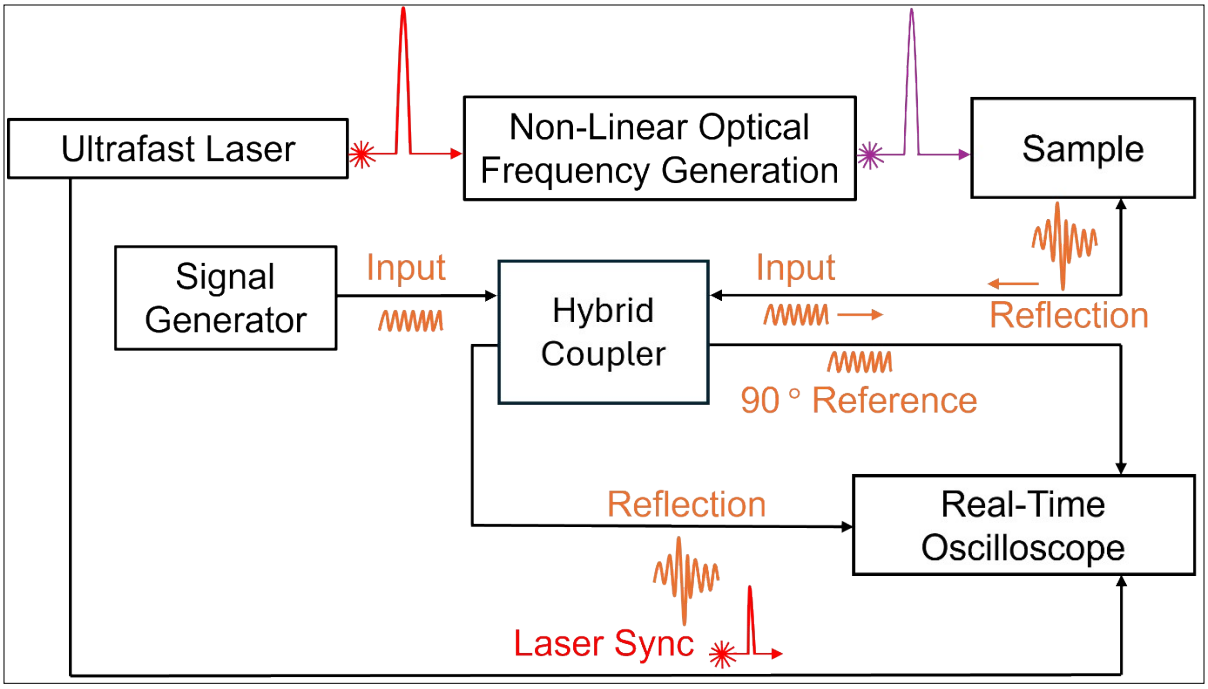

Figure S15. A diagram of the LUIS technique. A narrowband fs laser is generated by an ultrafast laser and, using non-linear optical techniques, a wide array of wavelengths can be generated. This light is then used to excite different dynamics within the LLTO, perturbing a GHz signal, which is being transmitted to the sample-pin interface via coaxial cables. The GHz signal is generated by a signal generator, routed through a hybrid coupler, reflected off the sample, which is perturbed by the laser, and then routed to the real-time oscilloscope, which is synced via a laser trigger from the ultrafast laser to set the time zero on the real-time oscilloscope.

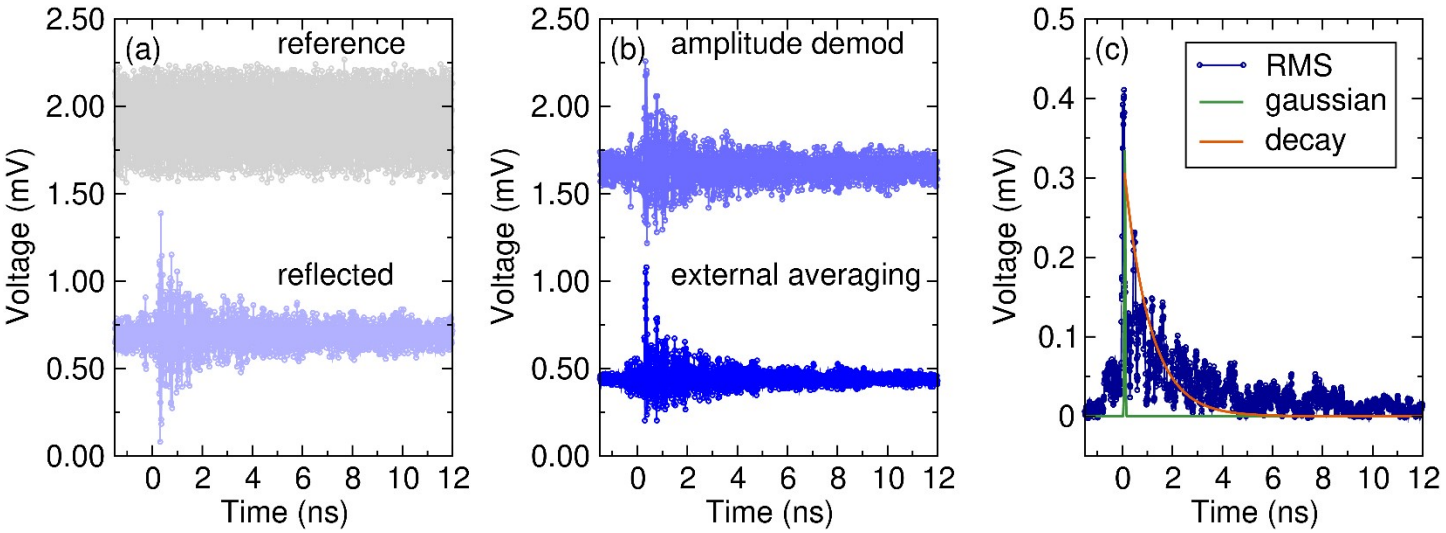

Figure S16. The processing steps for the extraction of the THz-LUIS signal beginning with (a) the reference signal collected from the 90° reference port in **Fig. S15** and the reflected signal routed to the oscilloscope from the perturbed sample, both averaged 1024 times. (b) The application of the oscilloscope's amplitude demodulation function and 1024 averages via the oscilloscope's math function. (c) The application of a root-mean-squared envelope function to the externally averaged signal in (b), as well as the gaussian rise and exponential decay components from the fitting model.

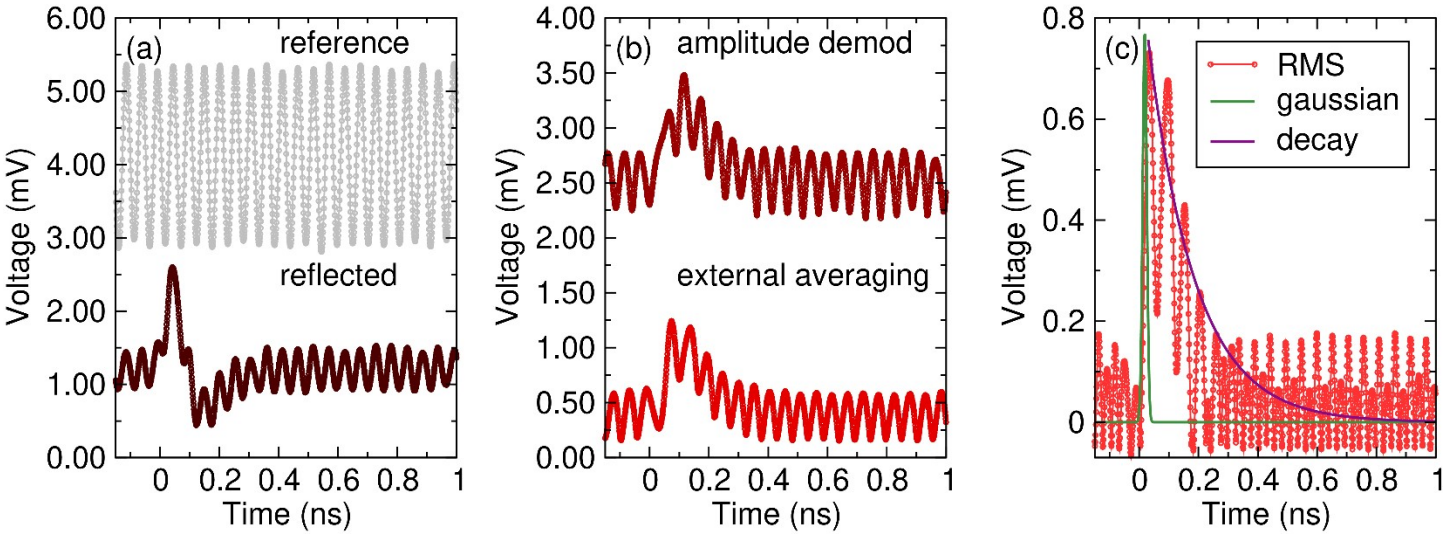

Figure S17. The processing steps for the extraction of the 800 nm-LUIS signal beginning with (a) the reference signal collected from the 90° reference port in **Fig. S15** and the reflected signal routed to the oscilloscope from the perturbed sample, both averaged 1024 times. (b) The application of the oscilloscope's amplitude demodulation function and 1024 averages via the oscilloscope's math function. (c) The application of a root-mean-squared envelope function to the externally averaged signal in (b), as well as the gaussian rise and exponential decay components from the fitting model.

Table S5. A summary of the rise time, or gaussian width (σ), and decay times (τ_d), reported with a 95% confidence interval, from the LUIS measurements. The fitting model is described in Equations 30-33 of the **Methods**.

Wavelength	σ **(ps)**	σ **Confidence Interval (ps)**	τ_d **(ps)**	τ_d **Confidence Interval (ps)**
800 nm	7.06	5.16-8.97	159	151-167
0.5-5.5 THz (54.5-599 μm)	20.5	19.0-22.6	1030	1000-1060

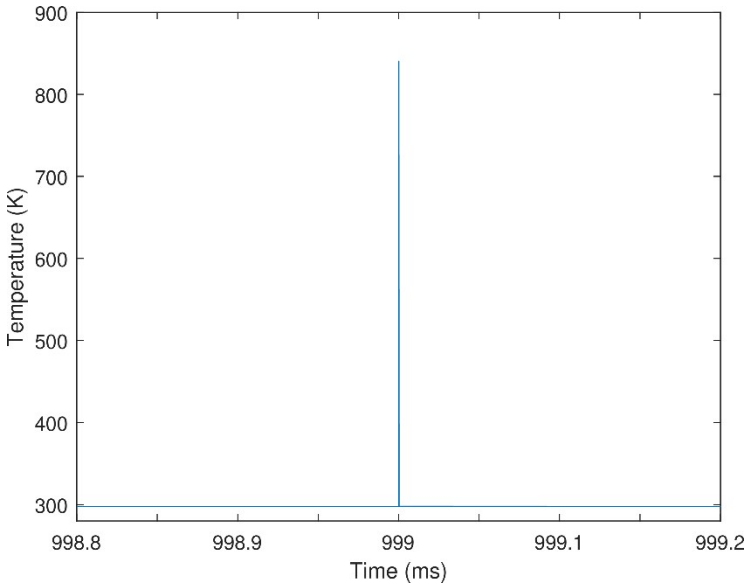

Figure S18. The peak temperature in the sample during and after the final pulse for the 800 nm, 20 mW light simulation. The nearly instantaneous rise and decay of heat occurs in less than 100 ns and is indicative of the extremely fast response induced by an ultrafast laser pulse.

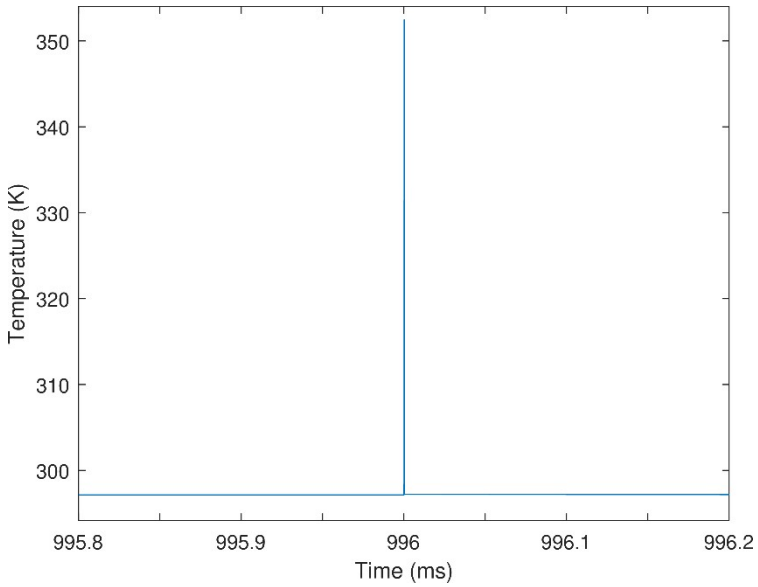

Figure S19. The peak temperature in the sample during and after the final pulse for the THz light simulation with 1 mW of laser power. The nearly instantaneous rise and decay of heat occurs in less than 100 ns and is indicative of the extremely fast response induced by an ultrafast laser pulse.

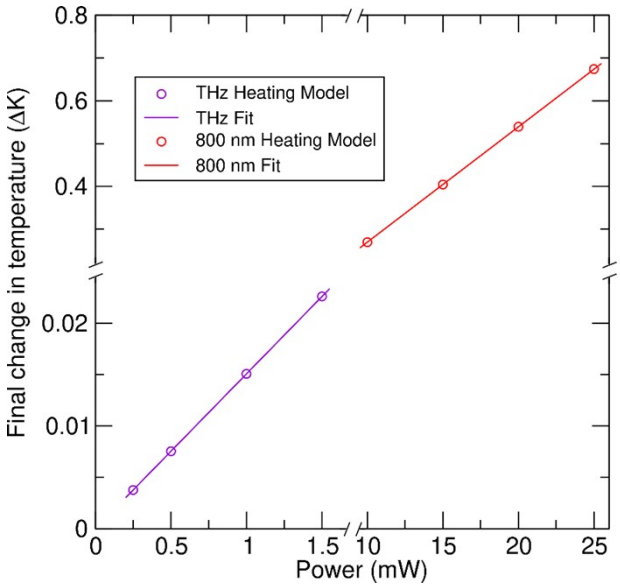

Figure S20. The final temperature of the sample due to optical heating as a function of average laser power for both the 800 nm and THz excitation in the range of excitation powers used experimentally. The final temperature is determined by taking the average maximum temperature at all time points during and after the final pulse. Our results suggest that the 800 nm excitation raises the sample temperature by 0.03 K per mW of power while the THz light raises the sample temperature by 0.02 K per mW of power.

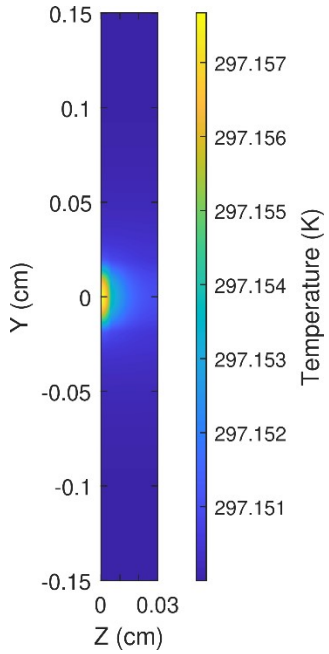

Figure S21. Cross-section of the sample after 1 s of ultrafast laser heating, modeled with a 1 mW THz light excitation with a penetration depth of 6 μm. The color bar corresponds to the temperature of the sample in Kelvin, with the initial temperature at 297.15 K. The sample and excitation are centered at x = 0 and y = 0.

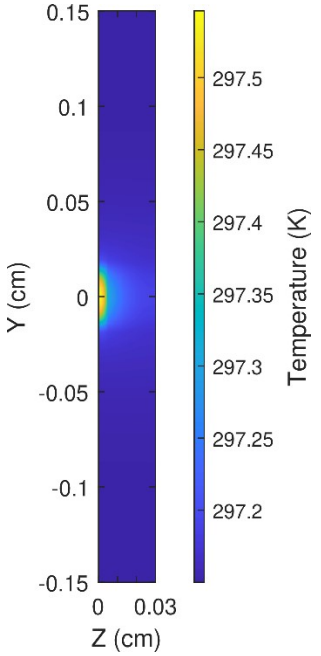

Figure S22. Cross-section of the sample after 1 s of ultrafast laser heating, modeled with a 20 mW 800 nm light excitation with a penetration depth of 7 μm. The color bar corresponds to the temperature of the sample in Kelvin, with the initial temperature at 297.15 K. The sample and excitation are centered at x = 0 and y = 0.

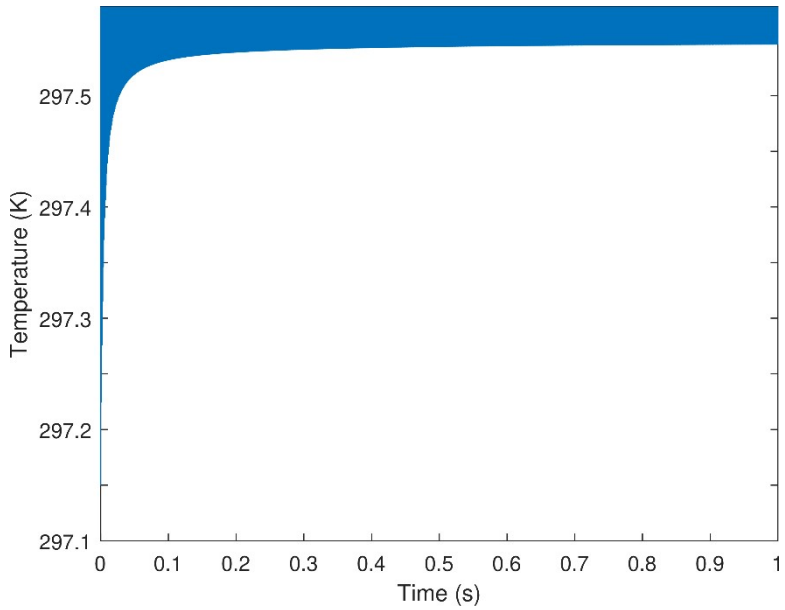

Figure S23. The baseline maximum temperature in the sample for 800 nm, 20 mW light. The simulation demonstrates that the sample's baseline temperature reaches steady state within one second. Each pulse still causes a nearly instantaneous rise and decay, but a steady baseline temperature of 297.55 K is reached within several tenths of a second.

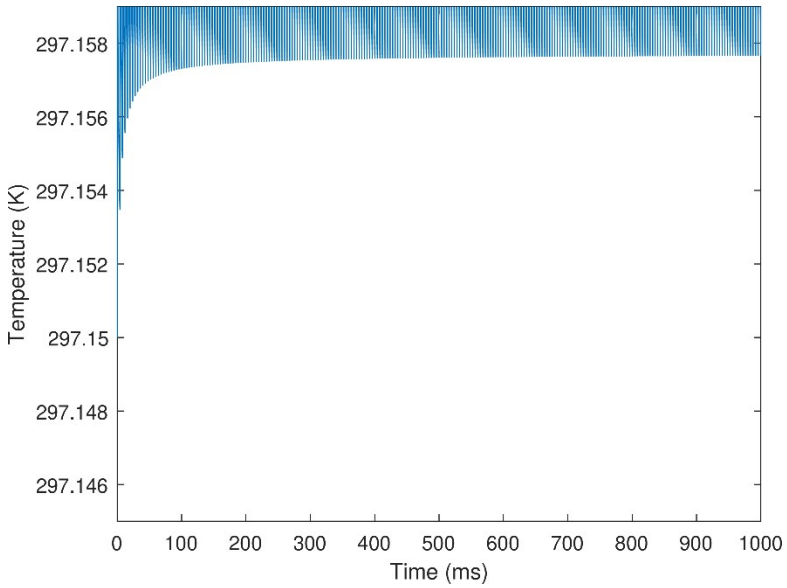

Figure S24. The baseline maximum temperature in the sample for 1 mW THz light. The simulation demonstrates that the sample's baseline temperature reaches steady state within one second. Each pulse still causes a nearly instantaneous rise and decay, but a steady baseline temperature of ~297.158 K is reached within several tenths of a second.

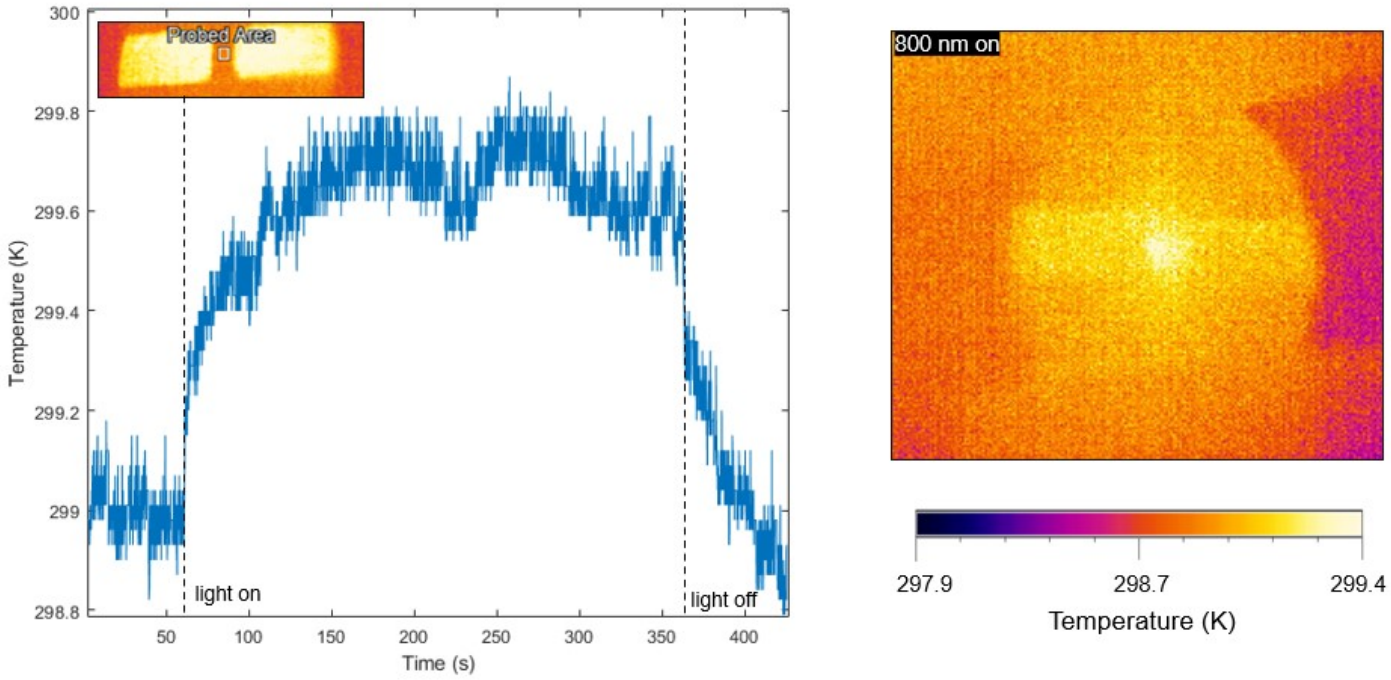

Figure S25. Experimental characterization of the sample's surface temperature under 800 nm, 20 mW light using an infrared thermal gun. Left: Surface temperature of the probed area upon illumination between 60 and 360 seconds. Right: Surface map of the sample with the 800 nm laser beam focused between the gold electrodes.

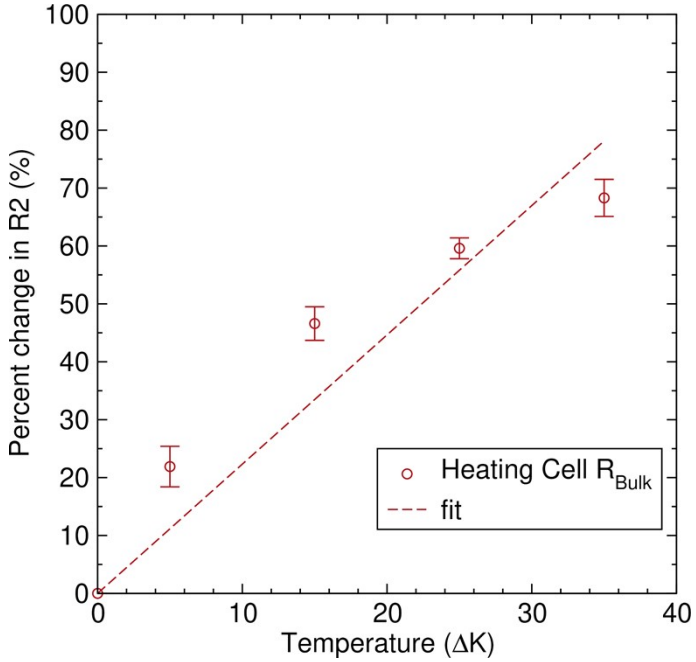

Figure S26. The percent change in impedance as a function of temperature. A 2.23% change in R_{bulk} correlates to a 1 K change ($R^2 = 0.9634$).

Table S6. Changes in the characteristic final temperature as the thermal conductivity is changed for the 20 mW 800 nm excitation.

Thermal conductivity ratio ($\kappa / \kappa_{nominal}$)	ΔT (K)
0.5	0.533
0.75	0.537
1	0.539
1.25	0.539
1.5	0.540

Table S7. Changes in the characteristic final temperature as the thermal conductivity is changed for the 1 mW THz light excitation.

Thermal conductivity ratio ($\kappa / \kappa_{nominal}$)	ΔT (K)
0.5	0.0150
0.75	0.0151
1	0.0150
1.25	0.0150
1.5	0.0151

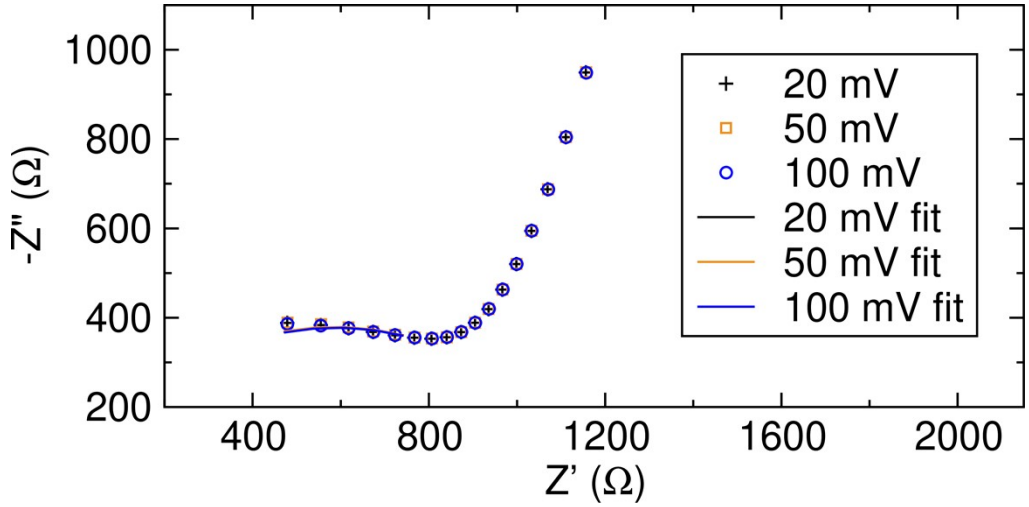

Figure S27. EIS performed at varied sinus amplitude between 20 and 100 mV, zoomed in to the bulk feature, demonstrating linearity due to the overlapping nature of the curves for each sinus amplitude.

Table S8. R_{bulk} values taken across three samples and three trials for each sinus amplitude in **Fig. S28**.

Sinus amplitude (mV)	R_{bulk} (Ω)	Standard deviation in R_{bulk} (Ω)
20	1132	55
50	1134	56
100	1142	55

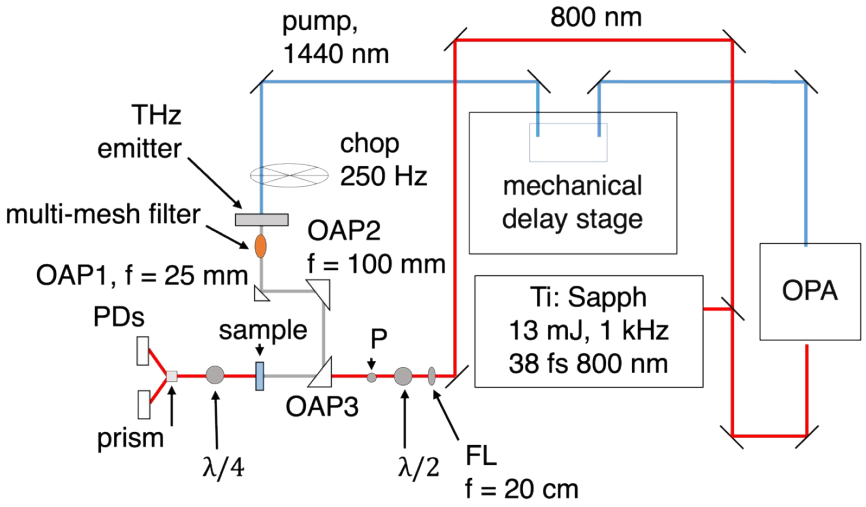

Figure S28. Diagram of the THz field set up. OPA: Optical Parameter Amplifier, OAP: Off-Axis Parabolic, FL: focal lens, P: polarizer, PDs: Photodiodes.

Table S9. IR power to THz field strength calibration yielding the average power calculation.

IR Pump Power (mW)	Field Strength (keV/cm)	Peak to Peak Voltage (V)	Average THz Power (mW)
1000	162.5	2.0	1.6
800	141.22	1.6	1.3
700	128.68	1.3	1.1
600	114.86	1.1	0.90
500	96.61	0.9	0.73
400	83.42	0.7	0.57
200	46.88	0.3	0.24

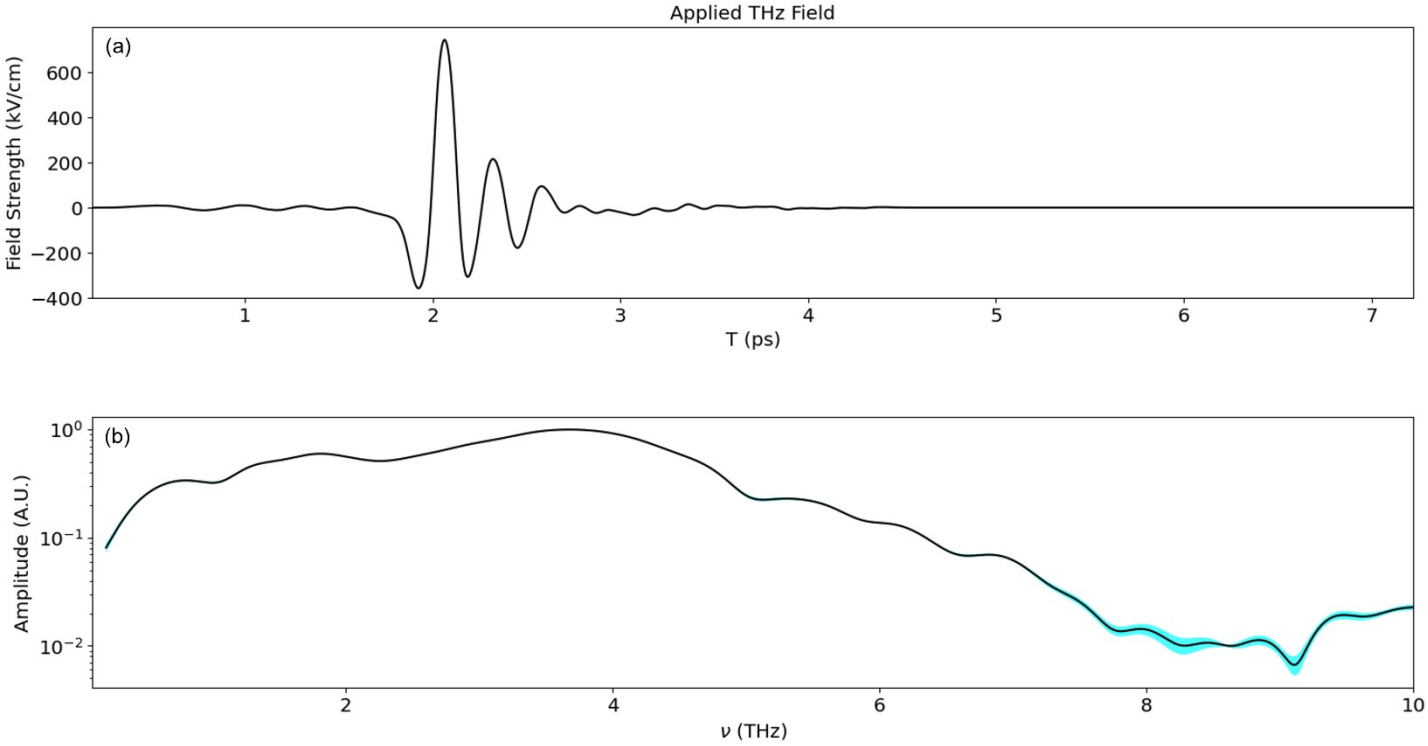

Figure S29. The (a) time domain trace of the applied THz field and (b) the frequency content of the same light, with uncertainties in the amplitude of the field shown, which was used to perturb the sample in the THz-LUIS experiment and was generated as described in the **Methods** section.

References:

(1) Catti, M.; Sommariva, M.; Ibberson, R. M. Tetragonal Superstructure and Thermal History of Li0.3La0.567TiO3 (LLTO) Solid Electrolyte by Neutron Diffraction. *J. Mater. Chem.* **2007**, *17* (13), 1300. https://doi.org/10.1039/b614345h.